Anatomic & metabolic brain markers of the m.3243A > G mutation: A multi-parametric 7T MRI study

Roy A.M. Haast[a,b,*], Dimo Ivanov[a], Rutger J.T. IJsselstein[c], Suzanne C.E.H. Sallevelt[d], Jacobus F.A. Jansen[e], Hubert J.M. Smeets[f,g,h], Irenaeus F.M. de Coo[c,g], Elia Formisano[a,b], Kâmil Uludağ[a,*]

[a] Department of Cognitive Neuroscience, Maastricht University, PO Box 616, 6200MD Maastricht, Netherlands
[b] Maastricht Centre for Systems Biology, Maastricht University, PO Box 616, 6200MD Maastricht, Netherlands
[c] Department of Neurology, Erasmus MC, Postbus 2040, 3000CA Rotterdam, Netherlands
[d] Department of Clinical Genetics, Maastricht University Medical Centre, PO Box 5800, 6202AZ Maastricht, Netherlands.
[e] Department of Radiology, Maastricht University Medical Centre and School for Mental Health and Neuroscience, Maastricht University, PO Box 5800, 6202AZ Maastricht, Netherlands
[f] Department of Genetics and Cell Biology, Maastricht University, PO Box 616, 6200MD Maastricht, Netherlands
[g] NeMo Expertise Centre, Postbus 2060, 3000CB Rotterdam, Netherlands
[h] Research School GROW, Maastricht University, PO Box 616, 6200MD Maastricht, Netherlands

ARTICLE INFO

ABSTRACT

One of the most common mitochondrial DNA (mtDNA) mutations, the A to G transition at base pair 3243, has been linked to changes in the brain, in addition to commonly observed hearing problems, diabetes and myopathy. However, a detailed quantitative description of m.3243A > G patients' brains has not been provided so far. In this study, ultra-high field MRI at 7T and volume- and surface-based data analyses approaches were used to highlight morphology (i.e. atrophy)-, microstructure (i.e. myelin and iron concentration)- and metabolism (i.e. cerebral blood flow)-related differences between patients (N = 22) and healthy controls (N = 15). The use of quantitative MRI at 7T allowed us to detect subtle changes of biophysical processes in the brain with high accuracy and sensitivity, in addition to typically assessed lesions and atrophy. Furthermore, the effect of m.3243A > G mutation load in blood and urine epithelial cells on these MRI measures was assessed within the patient population and revealed that blood levels were most indicative of the brain's state and disease severity, based on MRI as well as on neuropsychological data. Morphometry MRI data showed a wide-spread reduction of cortical, subcortical and cerebellar gray matter volume, in addition to significantly enlarged ventricles. Moreover, surface-based analyses revealed brain area-specific changes in cortical thickness (e.g. of the auditory cortex), and in T_1, T_2^* and cerebral blood flow as a function of mutation load, which can be linked to typically m.3243A > G-related clinical symptoms (e.g. hearing impairment). In addition, several regions linked to attentional control (e.g. middle frontal gyrus), the sensorimotor network (e.g. banks of central sulcus) and the default mode network (e.g. precuneus) were characterized by alterations in cortical thickness, T_1, T_2^* and/or cerebral blood flow, which has not been described in previous MRI studies. Finally, several hypotheses, based either on vascular, metabolic or astroglial implications of the m.3243A > G mutation, are discussed that potentially explain the underlying pathobiology. To conclude, this is the first 7T and also the largest MRI study on this patient population that provides macroscopic brain correlates of the m.3243A > G mutation indicating potential MRI biomarkers of mitochondrial diseases and might guide future (longitudinal) studies to extensively track neuropathological and clinical changes.

1. Introduction

The brain contributes to about 20% of the human body's energy consumption (Magistretti and Allaman, 2015; Sokoloff et al., 1977). Mitochondria serve as the biological units that utilize oxygen and glucose through oxidative phosphorylation to produce ATP from ADP (adenosine diphosphate). Approximately 4.7 billion ATP molecules per second are used by a single cortical neuron in a resting human brain, illustrating the extremely high energy demand of the brain (Zhu et al., 2012). As a result, a reduced energy production due to mitochondrial dysfunctioning may affect neuronal and glial integrity, leading to changes in the brain's structure and functioning (Keogh and Chinnery, 2015). For example, using MRI, qualitative cortical, white matter, brainstem and cerebellar morphological changes were observed in patients with respiratory energy chain defects (Saneto et al., 2008). In addition, changes are observed related to the homeostasis of biochemical compounds (such as iron, myelin and calcium), as particularly highlighted by deep gray matter MRI signal intensity changes (Dinopoulos et al., 2005).

Mitochondrial dysfunctioning can be caused by mutations in the mtDNA. Germline mutations can either occur de novo or be inherited from the mother. These mutations can be either homoplasmic, i.e. all mtDNA copies mutated, or heteroplasmic, i.e. a mixture of mutated and wild-type mtDNA. For heteroplasmic mutations, the mutation load may differ among different tissue types. As mitochondria are present in most eukaryotic cell types, mitochondrial mutations lead to a wide-range of symptoms, affecting multiple systems in the body, especially those with a high energy requirement, including the central nervous system (Lightowlers et al., 2015).

One of the most common mtDNA mutations is the m.3243A > G mutation within the mtDNA-encoded tRNA leucine 1 (*MTTL1*) gene (Goto et al., 1990), affecting proper incorporation of the amino acid leucine in mtDNA encoded proteins. The m.3243A > G mutation causes a broad variety of clinical manifestations, of which the MELAS or MIDD syndromes are the most common (i.e. 10% and 38% of m.3243A > G carriers, respectively). These patients are characterized by a wide range of phenotypic expressions, but most often suffer from sensorineural (due to dysfunctioning cochlear hair cells or nerve) hearing loss (51%), diabetes (42%) and proximal myopathy (27%) (Nesbitt et al., 2013). m.3243A > G specific brain symptoms are (transient) SLEs, visible as T_2 MRI signal hyperintensities and characterized by an increased CBF, as measured using ASL. Increased CBF is detected both before (Ikawa et al., 2013) and after onset of SLEs (Li et al., 2017), possibly to counterbalance observed neuronal hyperexcitability and pathology (Iizuka et al., 2002). Since SLEs are an important feature of the brain pathology in m.3243A > G patients, several studies have attempted to characterize the pathogenesis, as well as the temporal and spatial progression of these lesions. For example, these studies have shown locally increased lactate levels (Tsujikawa et al., 2010), but also a reduced apparent diffusion coefficient and cortical laminar necrosis (Iizuka et al., 2003). In addition, increased baseline CBF was observed in m.3243A > G patients without SLEs (Rodan et al., 2015).

However, not all patients fall within the 'standard' disease criteria, leading to sub-optimal and delayed diagnosis and prognosis. Several attempts have been made to link m.3243A > G mutation load in different tissue types (e.g. skeletal muscle, blood leukocytes and urine) with disease severity (based on, for example, number of symptoms or severity scores) to predict clinical prognosis (Chinnery et al., 1997; de Laat et al., 2012; Whittaker et al., 2009). Mutation load in UECs was preferred, based on its (1) strong correlation with clinical parameters, (2) stability throughout life and (3) non-invasive assessment. Based on the above criteria, it is evident that the m.3243A > G mutation induces a large diversity of symptoms, including different types of brain changes. While the severity of the phenotype may depend on mutation load, no previous study focussed on the mutation load-brain relationship in m.3243A > G patients. Thus, it is not clear how the mutation load is associated with cortical, subcortical and cerebellar pathologies on microscopic and macroscopic levels and how those relate to the individual's clinical symptoms.

In the present neuroimaging study, we aim to quantify the relationship between the m.3243A > G mutation load percentage and brain phenotype in a large group of patients (N = 22) and healthy controls (N = 15) using UHF 7T MRI. State-of-the-art quantitative brain imaging and analysis approaches are utilized that enable a direct comparison between groups and within patients, with a focus on the brain's morphological (e.g. brain volume and cortical thickness), microstructural-related (T_1 and T_2* relaxometry) and metabolism-related (CBF) properties. More specifically, we investigate (1) the relationship between (sub-)cortical and cerebellar atrophy with the m.3243A > G genotype (i.e. no mutation vs. low to high mutation load) and (2) the potential differences in myelin- and iron-sensitive T_1, T_2*, as well as CBF, colocalising with the morphological changes in patients.

The relative gain in SNR at 7T compared to clinical 1.5 T and 3 T depends on the MRI contrast used (Norris, 2003; Pohmann et al., 2016; Vaughan et al., 2001). For CBF using ASL the gain is approximately linear for high-resolution studies (e.g. below 2 mm isotropic). For example, in the study of Ivanov et al. (2017a), 7T outperformed 3 T by a factor of ~1.75 at 1.5 mm in-plane resolution for CBF data. For susceptibility contrasts, such as T_2* and functional MRI, the gain can be more than linear. Uludag and Blinder (2017) have theoretically estimated that the SNR of fMRI at high spatial resolution scales approximately quadratically with magnetic field strength. For T_1 contrast, however, a signal gain is only expected for very high resolution, higher than typically utilized in in vivo human studies.

Several studies already provided clear evidence of the enhanced detection of disease-specific morphological changes in the brains of, for example, multiple sclerosis and Alzheimer's disease patients using 7T compared to 3 T (Kollia et al., 2009; Nakada et al., 2008). Studies, comparing lower to UHF-MRI for a wide range of clinical applications, have been discussed recently by Trattnig et al. (2016). Here, the improved SNR for 7T enriches the images with spatial details not visible at lower field strengths due to the possibility to acquire data with a higher resolution and CNR, but without increasing the scan time (Duyn et al., 2007). As a result, 7T imaging exhibits increased diagnostic power due to enhanced sensitivity to detect fine-scale structural (Keuken et al., 2017; Stuber et al., 2014), perfusion (Gardener et al., 2009; Ivanov et al., 2017a) and functional (Pfeuffer et al., 2002; Uludag and Blinder, 2017; Yacoub et al., 2008) properties and changes in the brain, see also recent reviews by van der Zwaag et al. (2016) and Ugurbil (2017). As such, the current results contribute to a better understanding of the disease pathology and classification of m.3243A > G patients, in particular, and mitochondrial disease patients, in general.

2. Materials & methods

2.1. Participants

Twenty-two m.3243A > G patients and fifteen healthy age-, gender- and education-matched controls were included in this study after providing written informed consent in accordance with the Declaration of Helsinki. The protocol was approved by the ethics review board of the MUMC+ in Maastricht, The Netherlands. We included patients only when they were ADL-independent, as measured using the Barthel disability index and had a score < 30 on the NMDAS (Schaefer et al., 2006). We used three (current function, system specific involvement, and current clinical assessment) out of the four NMDAS sections, which resulted in a spectrum with less severe phenotypes to demonstrate the usefulness of quantitative MRI at 7T for detecting brain changes beyond lesions and atrophy, as it is typically assessed in imaging studies. For this reason, patients in the acute phase and/or with a history of SLEs were excluded. For severe phenotypes (i.e. Barthel index < 15 and/or NMDAS > 30), the brains of m.3243A > G patients strongly deviate
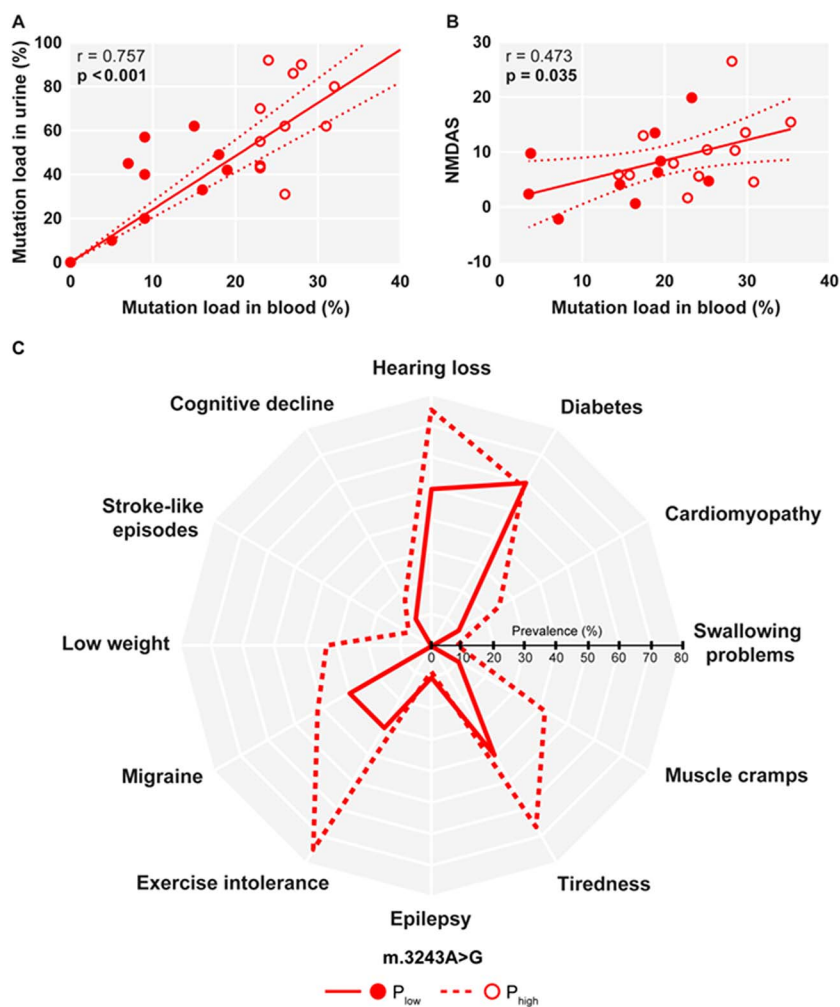
Fig. 1. Correlation analysis between clinical and genetic data. Scatter plots show the correlation between m.3243A > G mutation load (%) measured in UECs and blood (A) and the age- and gender-adjusted correlation between mutation load in blood and NMDAS score (B). Filled and empty dots represent P_{low} and P_{high} patients, respectively. Solid lines represent the best fit ± 95% CIs. Boldface p-values indicate a significant correlation. Spiderplot visualizes the prevalence of each symptom within both the P_{low} (solid line) and P_{high} (dashed line) m.3243A > G patient groups (C). Diabetes was true in case of known history from physician and HbA1c (IFCC) level higher than 45. Low weight was true in case of a BMI lower than 18.50.

from those of age-matched controls, already detectable with standard MRI methods at 1.5 and 3 T. Patients were only eligible for inclusion after evaluation of the clinically-relevant symptoms by an experienced clinician (I.F.M.d.C, see Fig. 1c for an overview of the symptoms). Patients with metallic implants (e.g. cochlear or stents) were excluded, as these would interfere with the magnetic field of the MRI scanner. Assessed parameters were: (1) m.3243A > G mutation loads (%) in blood and UECs following the procedure described in (Sallevelt et al., 2013), (2) fasting blood glucose (mmol/L) and HbA1c (% and IFCC) levels measured using standard procedures and (3) cognitive performance scores. Several cognitive domains were assessed using the visual 15-WLT to test memory, recall and recognition (Van der Elst et al., 2005), the Stroop colour-word test to test attention (Van der Elst et al., 2006b) and the LDST to test information processing speed (Van der Elst et al., 2006a). Raw test scores were Z-scored based on the average control scores for each cognitive task (see Table 1).

2.2. Data acquisition

MRI data were acquired using a whole-body 7T magnet (Siemens Medical Systems, Erlangen, Germany) and a 32-channel phased-array head coil (Nova Medical, Wilmington, MA, USA). High resolution (0.7 mm isotropic nominal voxel size) whole-brain quantitative T_1 and T_2^* images were obtained with MP2RAGE (Marques et al., 2010) and ME-GRE sequences, respectively. The SA2RAGE (Eggenschwiler et al., 2012) sequence was used to map B_1^+ across the brain. In addition to the anatomical scans, baseline partial-brain (excluding cerebellum and lower temporal lobes) perfusion was quantified using FAIR QUIPSS II

ASL (Ivanov et al., 2017b). The eye centers were taken as reference for the magnet isocenter position to improve the ASL labelling efficiency. See Supplementary Table 1 for the relevant sequence parameters. In addition, a standard dual-echo field map was acquired to correct the ASL data for EPI readout-related geometrical distortions. Dielectric pads containing a 25% suspension of barium titanate in deuterated water were placed proximal to the temporal lobe areas to locally increase the transmit B_1^+ field and to improve its homogeneity across the brain (Teeuwisse et al., 2012).

2.3. Surface-based analyses

Images were pre-processed to improve subsequent automatic volume- and surface-based processing. An extensive description of the pipeline can be found in the Supplementary Methods 1. The pre-processing included brain masking, *post-hoc* T_1 correction and computation of T_2^* and ASL maps. Cortical reconstruction and submillimeter volumetric segmentation was then performed with the FreeSurfer (v6.0, http://surfer.nmr.mgh.harvard.edu/) image analysis suite using the pre-processed MP2RAGE UNI images as input (Dale et al., 1999). Manual corrections of the tissue classifications were performed when necessary. Boundary-based registration (i.e. 'bbregister') was used to co-register the T_2^* and CBF maps to the MP2RAGE data with a 6 DOF transformation and spline interpolation. In addition, the fieldmap was used to correct for EPI readout geometrical distortions and improve the co-registration of the CBF map, particularly near the sinuses. Co-registered CBF maps were then corrected for partial volume effects by dividing it with a GM probability map obtained using SPM12 (http://

Table 1

Main characteristics of healthy controls and m.3243A > G patients. Values represent mean (± S.D.) if not stated otherwise. Significant differences between groups are indicated in bold-face.

	Controls (n = 15)	m.3243A > G patients (n = 22)	p-Value
Demographics			
Age, yr	38.40 (14.24)	41.23 (10.29)	0.487
Sex, % women	73.3	81.8	0.538
BMI, kg/m^2	24.43 (4.24)	23.04 (3.59)	0.289
Education, scale[a]	5.20 (1.21)	5.09 (0.92)	0.838
Glucose status			
Fasting glucose, mmol/L	4.99 (0.45)	6.56 (1.70)	**0.001**[b]
HbA1c, %	5.02 (0.64)	6.55 (1.24)	**< 0.001**[b]
HbA1c, IFCC	31.20 (7.21)	45.36 (12.40)	**< 0.001**[b]
Clinical-relevant symptoms			
Mutation load			
UECs, %	0	53.14 (26.09)	–
Blood, %	0	20.23 (11.40)	–
Barthel index	–	19.82 (0.83)	–
NMDAS	–	8.50 (4–13)	–
Number of symptoms	0	3.64 (2.46)	–
See Fig. 1C for more details			
Cognitive performance			
MMSE	29.13 (1.30)	28.27 (2.47)	0.226
LDST, z-score	0 (1.0)	−1.08 (2.18)	0.083
Stroop, z-score			
Words only	0 (1.0)	0.62 (1.35)	0.054
Colours only	0 (1.0)	0.95 (1.63)	0.081
Words and colours	0 (1.0)	1.40 (2.89)	0.127
15-WLT, z-score			
Total	0 (1.0)	−0.38 (1.04)	0.282
Recall	0 (1.0)	0.01 (0.99)	0.973
Recognition	0 (1.0)	−0.84 (3.01)	0.310

Abbreviations: BMI = body mass index; UEC = urinary epithelial cells; NMDAS = Newcastle Mitochondrial Disease Adult Scale; MMSE = mini-mental state examination; LDST = letter-digit substitution task; 15-WLT = 15-words learning task.

[a] Educational scale ranges from 1 (no education) to 8 (university).

[b] ANOVA, corrected for age, gender and BMI.

www.fil.ion.ucl.ac.uk/spm). For each subject, all modalities were projected onto the surface using FreeSurfer's mri_vol2surf function by averaging between 20 and 80% of the cortical thickness (with steps of 0.05%) to reduce potential partial voluming with WM and CSF. In addition, WM surface maps were computed by averaging between −0.5 mm and −2 mm distance (with steps of 0.05 mm) from the WM-GM boundary. All surface maps, including surface-based morphology metrics generated by FreeSurfer (e.g. cortical volume and thickness), were coregistered to the 'fsaverage' subject using sphere-based alignment (Fischl et al., 1999) and smoothed with FWHM = 10 mm for further statistical analyses. Final surface maps were visualized using the Connectome Workbench v1.2.3 viewer (Washington University School of Medicine, Saint Louis, MO, USA) after conversion of the inflated surfaces and overlays to a compatible format. Non-cortical tissue in between the hemispheres was masked using FreeSurfer's parcellation scheme to avoid inappropriate scaling of the surface maps.

2.4. Volume-based analyses

In addition to the surface-based data, volumetric data were assessed for subcortical structures and cerebellum. For the CN, GP and Pu, the automatic subcortical parcellation by FreeSurfer (Fischl et al., 2002) was manually corrected by taking into account the microstructural information (i.e. the values) from both the quantitative T_1 and T_2* maps using ITK-SNAP v3.6.0 (Yushkevich et al., 2006). In addition, RN, SN and DN were semi-automatically delineated, navigated by a threshold-based approach implemented in ITK-SNAP. The cerebellar segmentation tool (CERES) was utilized to accurately segment the cerebellum

into GM and WM (Romero et al., 2017). Final subcortical and cerebellar labels were used to export volume (mm^3) and average T_1, T_2* and CBF values for each of the structures to MATLAB and/or SPSS for further statistical analyses.

2.5. Statistical analyses

Descriptive participants' characteristics are reported as mean ± standard deviation (S.D.), while the median and IQR (25th and 75th percentiles) are shown for the NMDAS. Between-group (controls vs. m.3243A > G) demographic characteristics were tested by use of independent 2-sample t-tests (continuous data) or Pearson χ^2-tests (categorical data) with SPSS (Statistical Package for Social Sciences, version 23, IBM Corp., USA) and $\alpha = 0.05$.

For the volumetric data, a MANOVA test with Bonferroni correction was conducted to compare cGM, WM, subcortical GM (global or per structure) and cerebellar GM and WM volumes, T_1, T_2* and CBF between groups. Each patient was assigned to one of two groups based on mutation load. However, due to differences in mutation load across tissue types (and, in blood, also with age, see for example de Laat et al. (2012)), it is difficult to predefine the pathogenic threshold level (Chomyn et al., 1992) for brain tissue based on the blood and/or UEC data. Therefore, the median was used as classifier within the entire patient population. This was based on pragmatic reasons (i.e. to have equal sub-group sizes with comparable statistical power) in order to perform group-wise analyses (besides correlation). In addition, linear regression analysis was used to explore the relationship between mutation load and the structures volumes, T_1, T_2* and CBF, and was

therefore restricted to m.3243A > G patients. All tests were corrected for age, gender and eTIV.

For the cortical surface data, a two-step analysis approach was used, due to the high clinical variability between the m.3243A > G patients, for detection of (1) within- and (2) between-group brain differences. First, a whole-brain vertex-wise linear regression analysis was performed to detect clusters of vertices, for which cortical thickness (as measure of cortical atrophy), T_1, T_2* and CBF are significantly negatively or positively correlated with mutation load (in blood) in m.3243A > G patients. Here, age and gender were used as nuisance variables and corrected for multiple comparisons (i.e. number of vertices in left and right hemispheres) using Monte Carlo Null-Z simulation with a voxel-wise threshold of 2.0 (cluster-wise p-value of < 0.01). A more lenient cluster-wise p-value of < 0.05 was used for T_1, T_2* and CBF in a separate, additional analysis to also highlight subtle, but still significant, changes as a function of mutation load. This was motivated by the hypothesis that T_1, T_2* and CBF differences do not per se have to concur with, but can also pre- and/or proceed cortical thickness alterations. Second, significant clusters (per parameter) were then used to compare between groups using an ANOVA test, corrected for age and gender.

3. Results

The healthy control subjects (N = 15) were matched to the m.3243A > G patients (N = 22) on the basis of age (Pearson χ^2 test, p = 0.487), gender (p = 0.538) and educational level (p = 0.838), see Table 1. Significant higher fasting glucose (ANOVA, $F_{1,32} = 11.14$, p = 0.002) and HbA1c ($F_{1,32} = 12.75$, p = 0.001) levels were detected in m.3243A > G patients compared to controls, after accounting for age, gender and BMI (body mass index). The Barthel index was, except for one patient with a score of 16 (i.e. moderate to good self-supporting), maximal. Scores for the NMDAS ranged between 0 and 26 with a median score of 8.5 (IQR = 4–13).

3.1. m.3243A > G clinical characteristics

The mutation load in blood was significantly correlated with the mutation load in UECs (Pearson correlation, $r_{18} = 0.757$, p < 0.001, see Fig. 1A) and was on average 2.95 (± 1.40) times lower than in UECs. The median m.3243A > G percentage in blood of 23% was used to subdivide patients in P_{low} (< 23%, filled dots in Fig. 1A) or P_{high} (≥23%, empty dots). Correlation analyses revealed that both the mutation loads in blood ($r_{18} = 0.473$, p = 0.035, see Fig. 1B) and UECs ($r_{18} = 0.550$, p = 0.012, not shown) are positively correlated (after correcting for age and gender) with the NMDAS score. Increasing mutation load in blood, not UECs, was correlated with worse cognitive test performances for the LDST (Pearson correlation, $r_{18} = -0.745$, p = 0.005) and Stroop tasks ($r_{18} = 0.599$, p = 0.025, not shown), corrected for age, gender and education.

Hearing loss was the most prevalent observed symptom within the m.3243A > G patient group (P_{low} vs. P_{high}: 50 vs. 75%), as can be observed in Fig. 1C. This was followed by diabetes mellitus (60 vs. 58.3%), exercise intolerance (30 vs. 75%) and tiredness (40 vs. 66.7%). Migraine (30 vs. 41.7%) and muscle cramps (10 vs. 41.7%) are moderately observed, while cardiomyopathy (10 vs. 25%), underweight (0 vs. 33.3%), cognitive decline (10 vs. 16.7%), epilepsy (10 vs. 8.3%), swallowing problems and SLEs (both 0 vs. 8.3%) are only observed in few patients. There was a significantly higher prevalence of exercise intolerance (Pearson χ^2 test, p = 0.035) in the P_{high} group compared to the P_{low} group.

3.2. Global brain morphology

Example quantitative T_1, T_2* and CBF maps for a control subject and an m.3243A > G patient of comparable age (66 vs. 67 yrs. old) are depicted in Fig. 2 across several axial slices. Note that, because we acquired quantitative MRI parameters, we can choose the same absolute scale for all subjects allowing us to examine quantitative MRI differences in addition to local contrast differences, typically indicative of lesions and atrophy. Clear signs of WMLs (see dashed blue box) were visible in both the patient's T_1 and T_2* maps and were characterized by increased T_1 and T_2* relaxation times. In addition, a larger sulcal cerebrospinal fluid volume (i.e. increased space between neighboring gyri) was visible for the patient, suggesting gray and/or white matter volume loss. In addition, with respect to the cerebellum, larger inter-folial spaces were visible for several patients (not shown). Possible differences regarding (sub)cortical perfusion (bottom row) were more difficult to detect visually and needed quantitative analysis. Therefore, we examined the normalized T_1, T_2* and CBF distributions for both cGM and WM tissue. Both cGM and WM T_1 showed a significant increase as a function of mutation load (see Supplementary Fig. 1).

The total volume (in mm^3, including left and right hemispheres, corrected for eTIV) was computed for each structure (cGM, ventricles, subcortical GM and cerebellar GM, see Figs. 3A-D, respectively) to characterize the morphological differences between groups. WM and cerebellar WM volumes are shown in Supplementary Fig. 2A and B, respectively. Significantly different brain volumes were detected across groups (MANOVA, Wilks' Lambda = 0.438, $F_{12,54} = 2.298$, p = 0.019). Here, the cGM as well as the WM volume were significantly different between groups ($F_{2,32} = 7.783$, p = 0.002 and $F_{2,32} = 5.090$, p = 0.012, respectively). Similarly, group differences were observed for the ventricles ($F_{2,32} = 4.101$, p = 0.026) and subcortical ($F_{2,32} = 5.670$, p = 0.008) and cerebellar GM ($F_{2,32} = 8.506$, p = 0.001) volumes, but not for the cerebellar WM volume. Significant differences were only found when comparing the control subjects with the P_{high} group (p = 0.002 for cGM, p = 0.010 for WM, p = 0.024 for the ventricles, p = .035 for subcortical GM, p = 0.001 for cerebellar GM) but not with the P_{low} group, except for the subcortical GM (p = 0.021). Significant correlations were observed between mutation load and each structure's volume (Pearson correlation, $r_{18} = -0.282$, p = 0.005 for cGM, $r_{18} = -0.228$, p = 0.024 for WM, $r_{18} = -0.604$, p = 0.008 for the ventricles and $r_{18} = -0.074$, p = 0.008 for cerebellar GM) across patients, except for the subcortical GM and cerebellar WM. Note that we did not correct for fasting glucose status, as this did not significantly affect the structures' volume within the patient group. Finally, no differences were observed across groups with regards to eTIV.

3.3. Fine-scale cortical morphology, microstructure and perfusion

Several cortical ROI clusters of vertices showed a significant (cluster-wise p-value of < 0.01) negative correlation between cortical thickness and mutation load in blood, see Fig. 4A (delineated by yellow lines). In general, the clusters encompassed regions predominantly within (respective to the FreeSurfer's annotation) the middle frontal gyri, parietal (including precuneus) and superior temporal lobes. Strikingly, no significantly correlated clusters remained after multiple comparison correction when repeating the same analyses using mutation load in UECs. Similar analyses were performed using T_1, T_2* or CBF instead of cortical thickness (see Fig. 4B–D, respectively). T_1 and T_2* increased as a function of mutation load (cluster-wise p-value of < 0.05) in pre- and post-central sulci, as well as in the occipital lobes, precuneus and insula for T_2*. Increasing CBF was found in the superior frontal sulcus. To visualize the overlap of the findings using the different MRI modalities, significant clusters (vertex-value = 1) were summed and color-coded, ranging between 1 (green)-4 (purple), see Fig. 4E. Most overlap was observed near the central sulci, frontal gyri, occipital lobes and precuneus.

Z-scores were computed per cluster for each parameter and subsequently averaged to compare across groups. Group-wise averages revealed a significant lower cortical thickness in the m.3243A > G
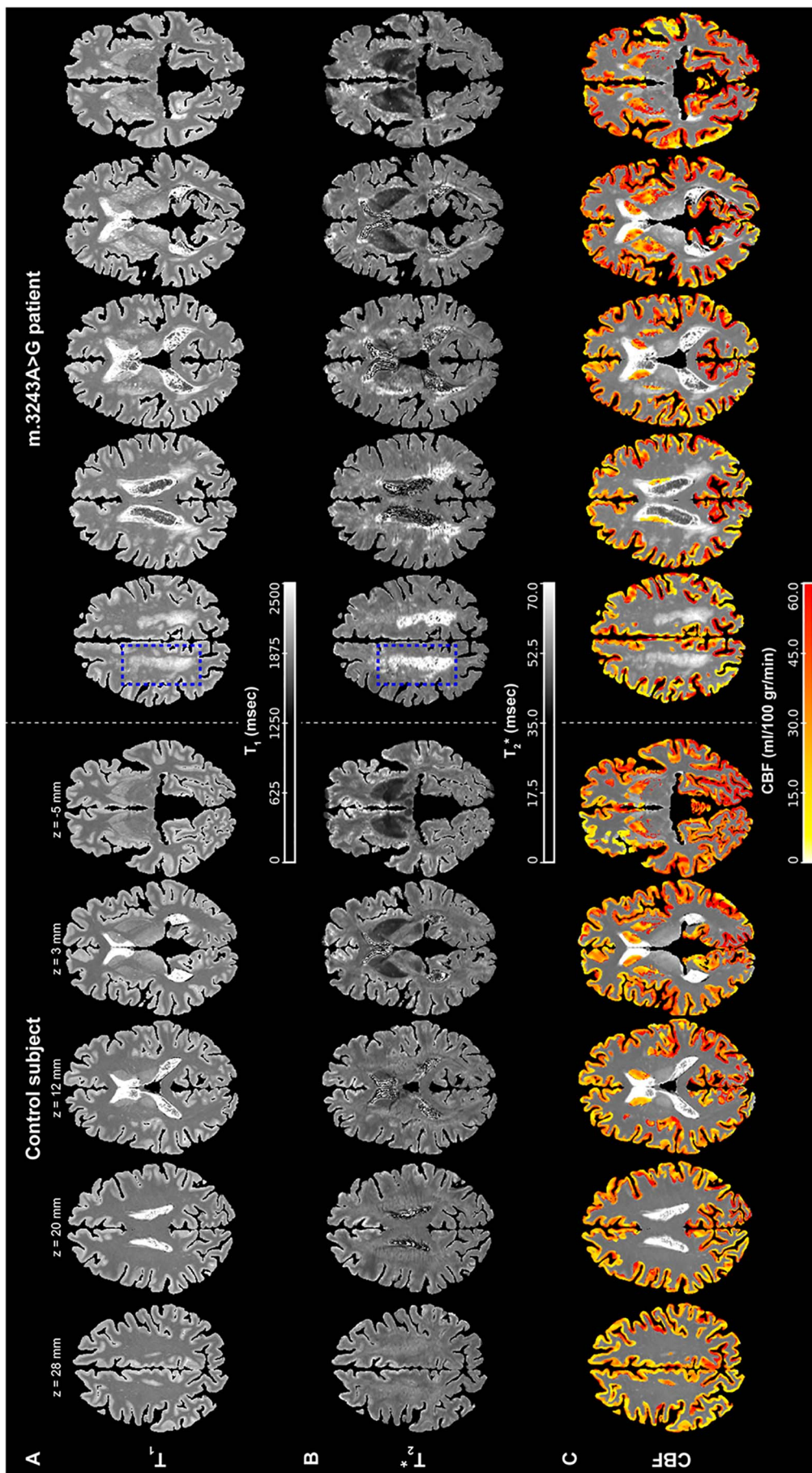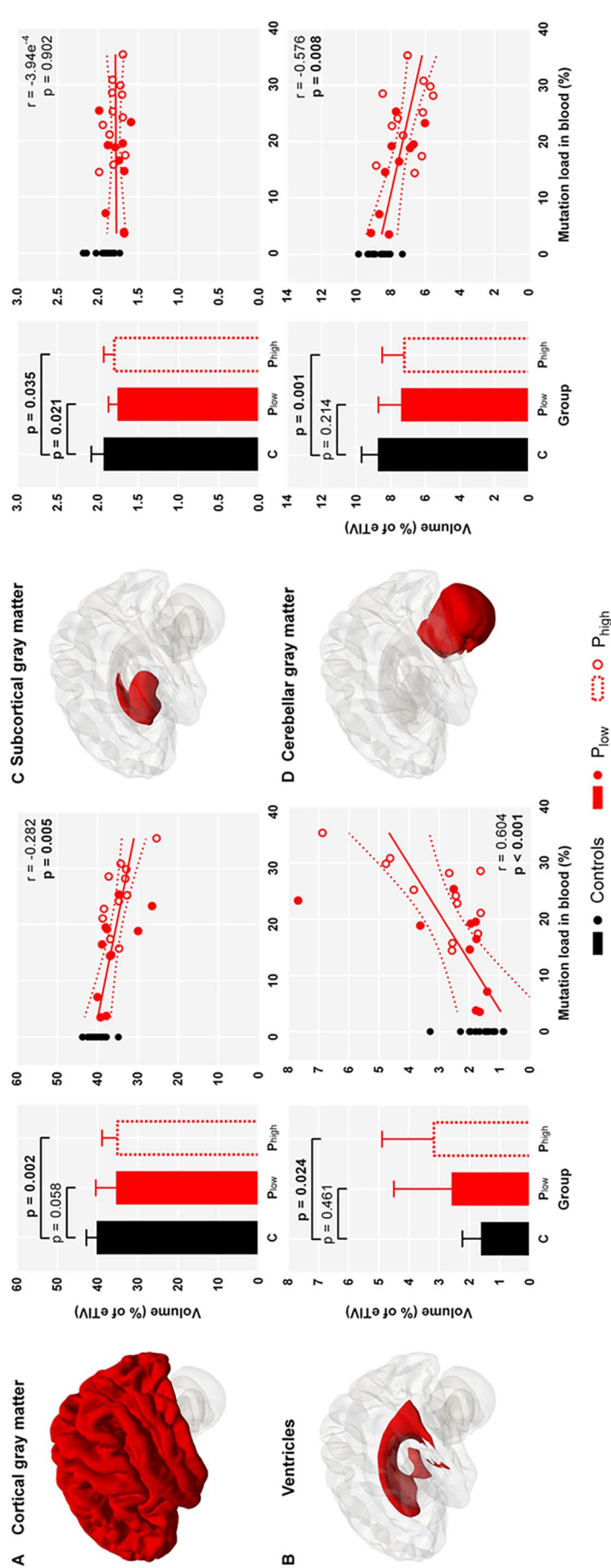
Fig. 2. Example MRI data. T_1 (msec, A), T_2^* (msec, B) and CBF (ml/100 g/min, overlaid onto the T_1 map, C) maps are shown for a single control subject (left, age = 66 yr, M) and m.3243A > G patient (right, age = 67 yr, F). White matter lesions are highlighted by the dashed blue box and z-coordinates are shown (MNI-space) as reference.

Fig. 3. Between and within (i.e. mutation load effect) group comparison of the brain structure's volumes. Bar plots display unadjusted mean (± S.D.) volumes for total gray matter (A), ventricles (B), subcortical (C) and cerebellar (D) gray matter volumes for controls (black) and P_{low} (filled red) and P_{high} (dashed red bars) mutation load in blood. Boldface p-values indicate a significant difference between groups after correction for age, gender and multiple comparisons. Scatterplots show the correlation between volume and mutation load in blood for m.3243A > G patients (P_{low}: filled and P_{high}: empty red dots), adjusted for age and gender. Mean volume for each control subject (black dots) are displayed for reference and red solid lines represent the best fit ± 95% CIs. Boldface p-values indicate a significant correlation between mutation load in blood and volume after correcting for age and gender. (For interpretation of the references to color in this figure legend, the reader is referred to the web version of this article.)
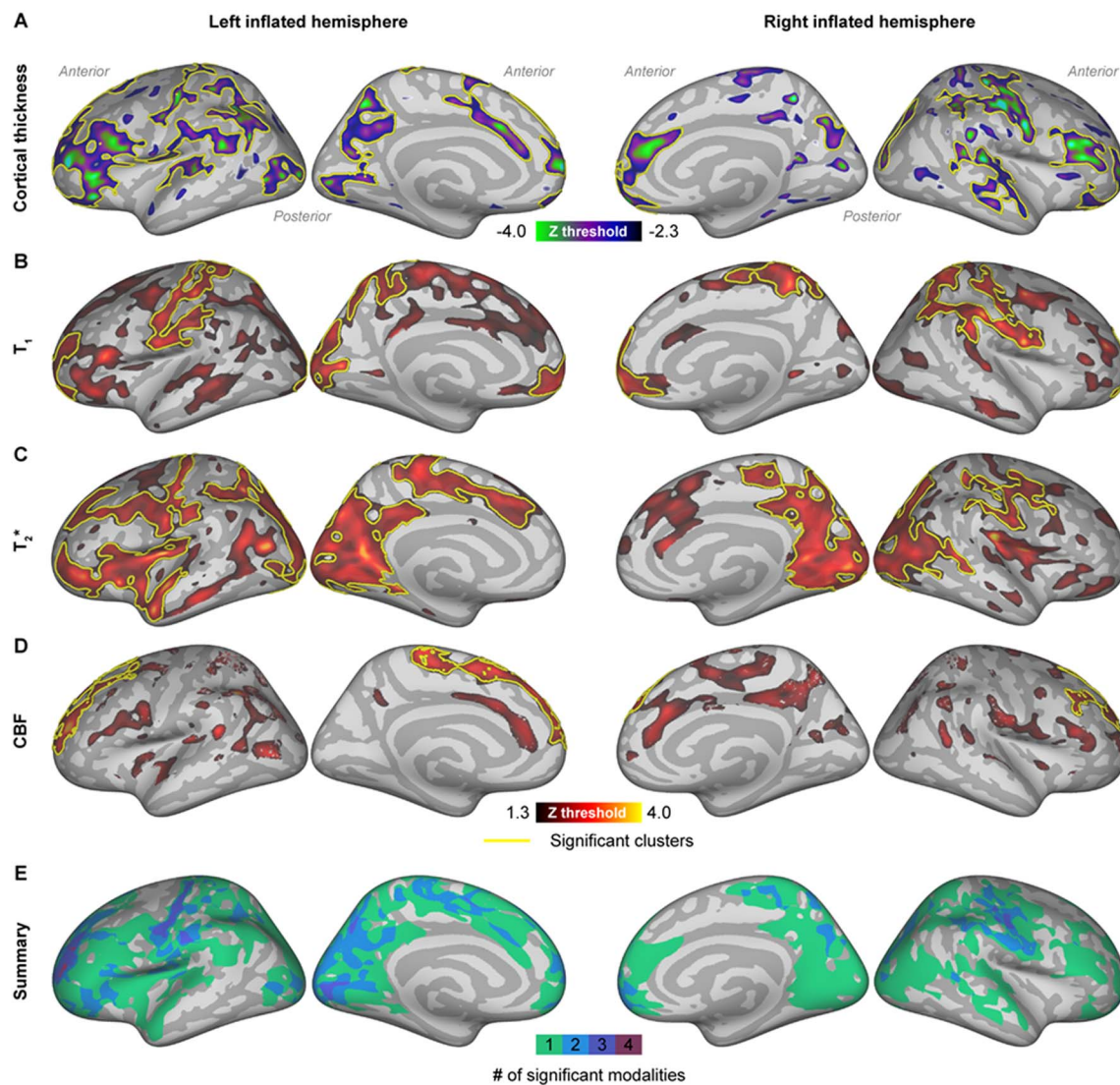
Fig. 4. Surface-based MRI data analysis. Vertex-wise linear regression analyses between mutation load in blood and cortical thickness (A), T_1 (B), T_2^* (C) and CBF (D) within the m.3243A > G patients. Statistical z-maps, overlaid onto the left and right inflated (unfolded) surface reconstructions, show the vertices where cortical thickness (negatively), T_1, T_2^* or CBF (positively) correlated with mutation load (after correction for age and gender). Significant clusters that remained after cluster-wise multiple comparison correction are delineated by yellow borders. Clusters were summarized across parameters by color-coding (1, green, to 4, purple) vertices based on the number of significant clusters (E). (For interpretation of the references to color in this figure legend, the reader is referred to the web version of this article.)

patients (including both P_{low} and P_{high} patients, ANOVA, $F_{1,33} = 5.646$, p = 0.023) compared to controls (see Fig. 5A). No significant differences were observed across groups for the T_1, T_2^* and CBF data (see Fig. 5B–D), but compared to the controls, lower T_1 was observed for P_{low}, while a slightly higher T_1 is observed for P_{high}. A similar, but less apparent, pattern was observed for the T_2^* and CBF data.

Analogous to cGM, subcortical (i.e. alongside the cGM clusters) WM T_1 and T_2^* were compared across groups (see Supplementary Fig. 2A). WM T_1 and T_2^* were not significantly different across groups. However, WM T_2^* increased with mutation load in blood within the m.3243A > G patients (Pearson correlation, $r_{18} = 0.454$, p = 0.044). Similarly, a trend was observed for WM T_1 ($r_{18} = 0.421$, p = 0.065).

3.4. Subcortical and cerebellar morphology, microstructure and perfusion

Reduced subcortical GM volume was observed for both the P_{low} and P_{high} groups compared to the controls, but no effect of mutation load (see Fig. 3D). Group-averaged volumes for each subcortical structure (see Fig. 6A) individually are plotted (see Fig. 6B) and highlights significantly reduced volume in the m.3243A > G patients compared to
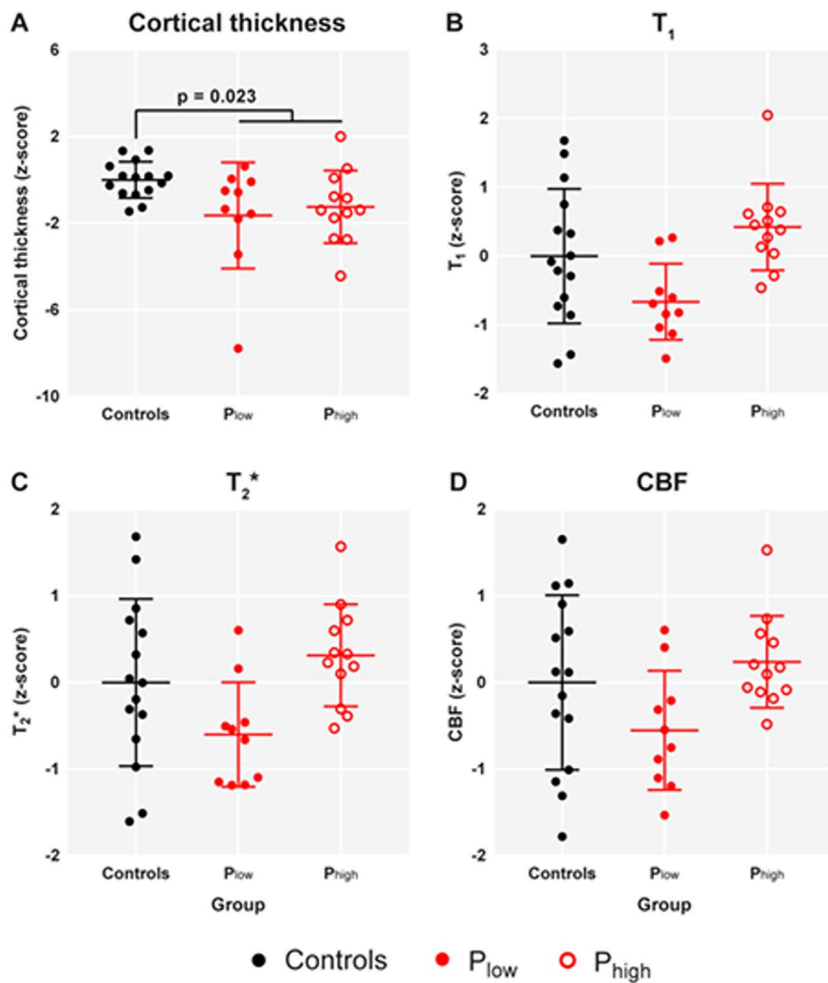
controls (MANOVA, Wilks' Lambda = 0.616, p = 0.025) for the Pu ($F_{1,33} = 8.959$, p = 0.005) and GP ($F_{1,33} = 4.621$, p = 0.039). No clear microstructural changes, i.e. between groups or as function of mutation load, in the subcortical structures were present. However, several patients showed signs of spongiotic lesions in the Pu and GP that were characterized by high T_1 and T_2^*, locally (see for example Fig. 6A for one subject). CBF increased with mutation load (Pearson correlation, $r_{18} = 0.489$, p = 0.029).

More pronounced effects were observed for cerebellar GM (see Fig. 7). Here, T_1 was significantly higher for m.3243A > G (ANOVA, $F_{1,33} = 12.947$, p = 0.001) and especially for the P_{high} group compared to controls ($F_{2,32} = 9.915$, p < 0.001, see Fig. 7A, top row). Moreover, T_1 increases as a function of mutation load ($r_{18} = 0.485$, p = 0.030, see Fig. 7B). In contrast, T_2^* was comparable across groups and did not correlate with mutation load. Similar but fewer significant findings were shown for cerebellar WM (see Supp. Fig. 2B).

4. Discussion

Mitochondrial dysfunctioning, either induced by acquired damage

throughout life (such as by nucleases and reactive oxygen species) and/ or by de novo or maternally inherited germline variations of the mtDNA, has been consistently linked to neurodegeneration (Keogh and Chinnery, 2015). While several mtDNA mutations are known to affect the brain (Reeve et al., 2008), the current study focussed on the effects of the m.3243A > G genotype (i.e. mutation load) on the brain tissue using multiple parametric maps acquired with 7T MRI and compared these data to values obtained on healthy controls.

4.1. Mutation load and clinical characteristics

In the current study, we assessed mutation loads in both UECs and blood. Despite the mutation load in blood (leukocytes) being significantly lower compared to that in UECs, albeit comparable to that observed in earlier studies (Fayssoil et al., 2017; Shanske et al., 2004; Whittaker et al., 2009), both measures strongly correlated (de Laat et al., 2012; Frederiksen et al., 2006). It is known that the mutation load in blood decreases over lifetime with a constant rate of 1.4% per year (Rahman et al., 2001), while the mutation load in UECs is considered to be more consistent with age. Here, the loss of the m.3243A > G mutation in blood presumably originates from a selection against pathogenic mtDNA mutations in a stem cell population (Rajasimha et al., 2008).

Hearing loss was the most prevalent symptom within the current study population, followed by exercise intolerance and diabetes mellitus. This matches with the MELAS and MIDD-like phenotypes associated with the m.3243A > G mutation and is in line with previous findings, reporting comparable numbers across their study cohorts (de Laat et al., 2012; Fayssoil et al., 2017; Nesbitt et al., 2013). In addition,

we found a significant correlation between mutation load (in blood and UECs) and NMDAS score, as also shown in previous studies (de Laat et al., 2012; Whittaker et al., 2009). The observed differences between the P_{low} and P_{high} groups in terms of symptoms prevalence, especially in the myopathy-related symptoms (e.g. exercise intolerance), can partly be explained by the "mitochondrial threshold effect" (Rossignol et al., 2003). The significant correlation between the proportion of apoptotic muscle fibers and the proportion of mutant mtDNA exemplifies this hypothesis (Aure et al., 2006). It is known that the mitochondrial copy number can compensate and can be increased by physical exercise, implying the mutation load is not the only factor involved. Like muscle cells, neurons are post-mitotic and therefore are likely to behave similarly. Comparable mutation loads were detected across several brain regions to those in skeletal muscle. However, it is not known how the mutation load in neurons develops over lifetime (Betts et al., 2006). We have found that the mutation load in blood is a better marker for cognitive performances and brain functioning in m.3243A > G patients than the mutation load in UECs, even though both mutation loads are correlated to each other. The reason for this discrepancy is unknown, but may be specific to the age-range of the current patient population.

4.2. Brain morphological markers of the m.3243A > G mutation

The current results present strong evidence of a mutation load effect within the patient population on global brain volume, in addition to widespread lower brain volume in the patients compared to controls. While patients with a low mutation load are characterized by normal-appearing brains, stronger brain atrophy is observed in patients with higher mutation load. This was especially apparent in the cortical and
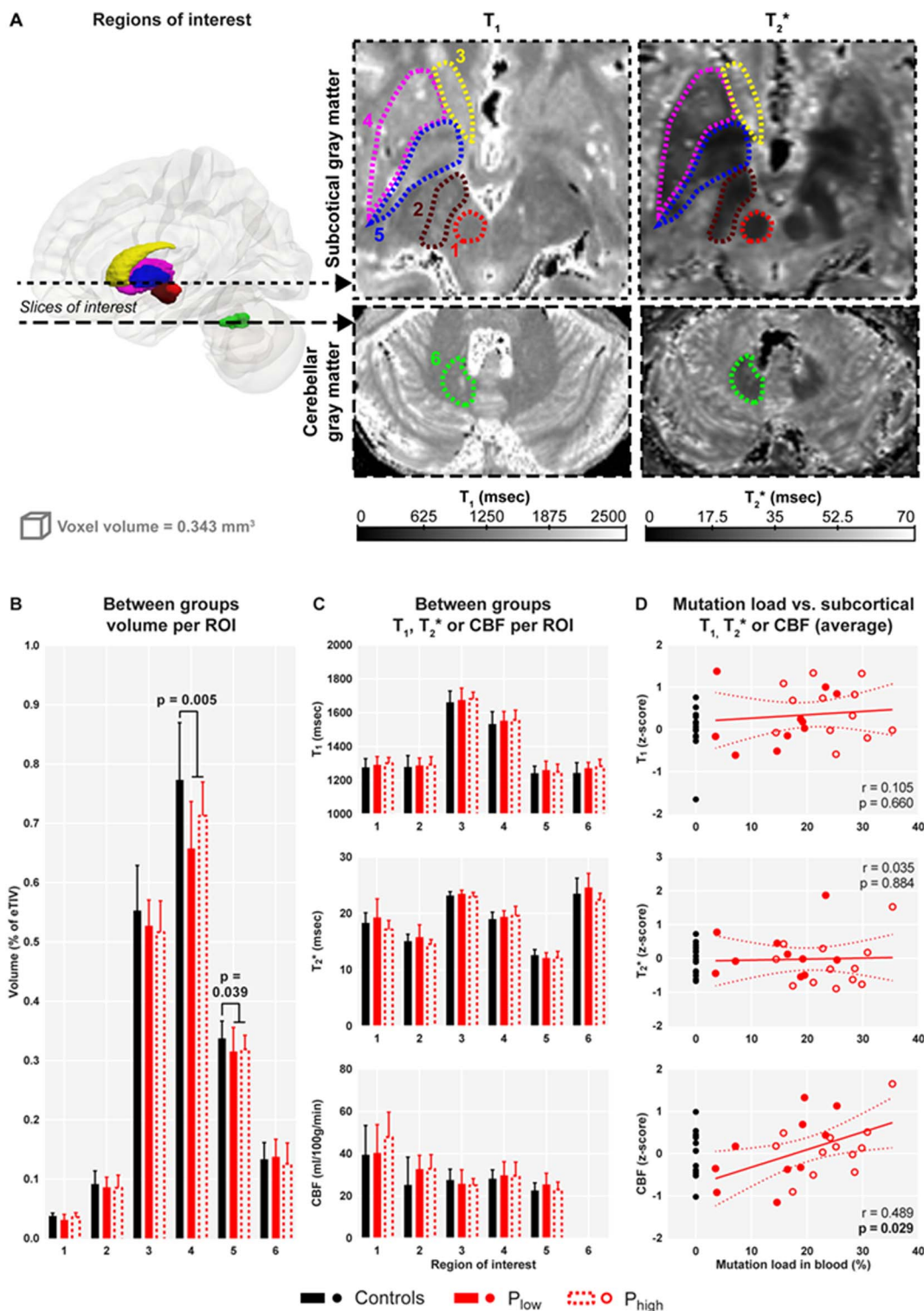
Fig. 6. Between and within group comparison of subcortical structures. ROIs (1 = RN, 2 = SN, 3 = CN, 4 = Pu, 5 = GP and 6 = DN) are displayed schematically in A. Mean subcortical gray matter volume (B) and T_1, T_2* and CBF (C) are compared across groups (controls: filled black, P_{low}: filled red and P_{high}: dashed red bars) per ROI. Scatterplots display the correlation between mean (z-scored relative to controls and averaged across ROIs) T_1, T_2* and CBF vs. mutation load in blood (D). Mean values for controls (black dots) are displayed for reference and red solid lines represent the best fit ± 95% CIs. Boldface p-values indicate a significant correlation between mutation load in blood and cortical thickness, T_1, T_2* or CBF after correction for age and gender. (For interpretation of the references to color in this figure legend, the reader is referred to the web version of this article.)

cerebellar GM, but not for the subcortical structures, which is in accordance with biochemical analyses of post-mortem brains (Sparaco et al., 2003). Strongest local cGM atrophy and reduced cortical thickness as a function of m.3243A > G mutation load was observed in regions linked to: (i) auditory processing (superior temporal cortices), (ii)

attentional control (middle frontal and parietal gyri and anterior cingulate cortices), (iii) sensorimotor network (central sulci and neighboring gyri) and (iv) default mode network (precuneus). These latter two structures were also observed by a recent study that used voxel-based morphometry to characterize morphological differences between
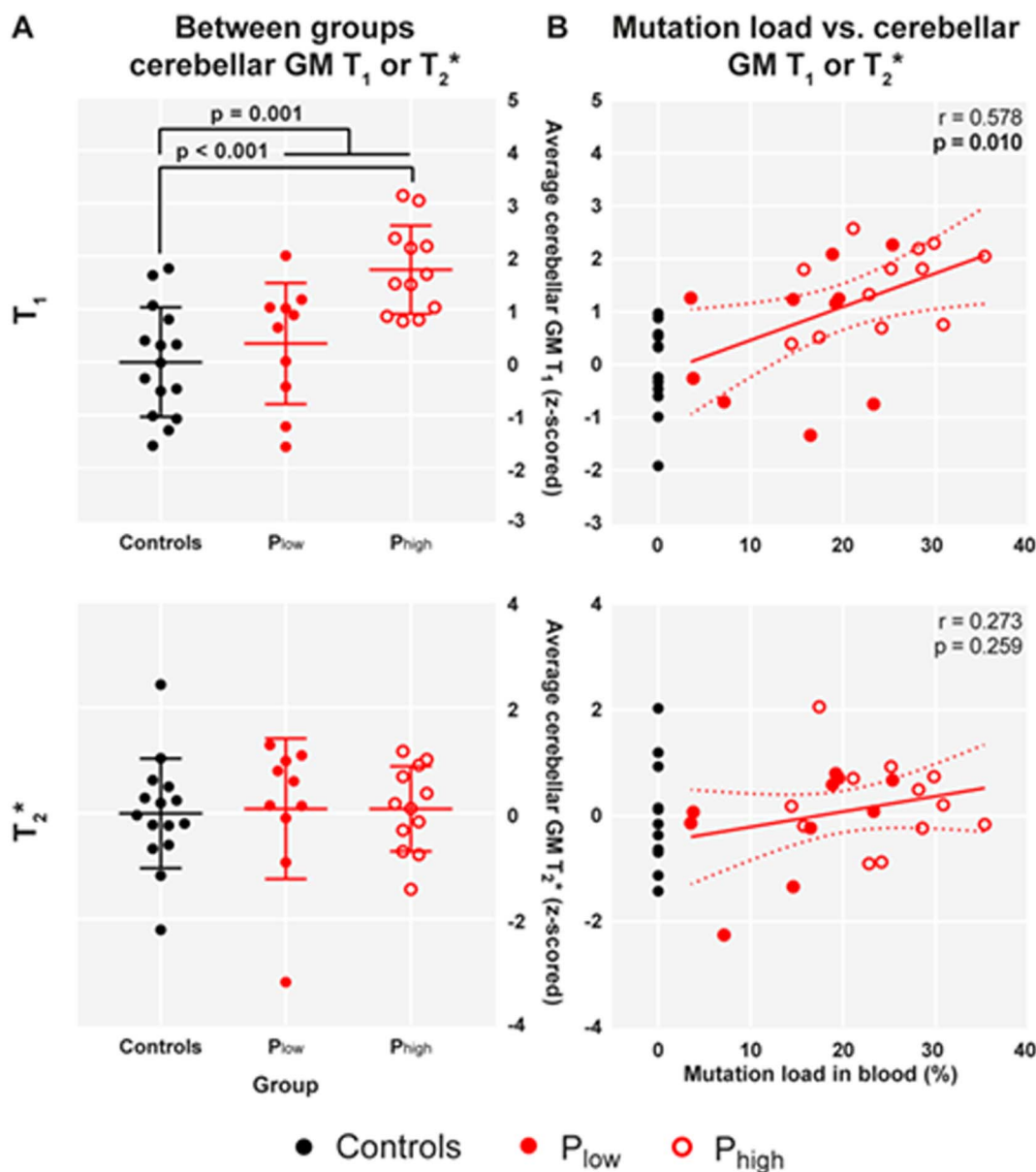
Fig. 7. Between and within group comparison of cerebellar GM. Dot plots in A display unadjusted mean (± S.D.) cerebellar GM T_1 (top) or T_2* (bottom) values for controls (black), P_{low} (filled red) and P_{high} (empty red dots). Boldface p-values indicate a significant difference between groups after correction for age, gender and multiple comparisons. Scatterplots in B show the correlation between T_1 or T_2* and mutation load in blood for m.3243A > G patients (P_{low}: filled and P_{high}: empty red dots), adjusted for age and gender. Mean T_1 or T_2* for each control subject (black dots) are displayed for reference and red solid lines represent the best fit ± 95% CIs. Boldface p-values indicate a significant correlation between mutation load in blood and cerebellar T_1 or T_2* after correction for age and gender. (For interpretation of the references to color in this figure legend, the reader is referred to the web version of this article.)

m.3243A > G patients and healthy controls (Tsujikawa et al., 2016). Notably, significant local correlations, after correction for multiple comparisons, between cortical thickness and mutation load were only found for values from the blood.

The neuropathological effects of the mutation load in some brain areas, but not in others, signify the differential abilities of neurons to survive respiratory chain deficiencies (Betts et al., 2006). More work has to be performed, particularly using invasive cellular methods, to establish the link between mitochondrial dysfunction and macroscopic brain changes, as detected with non-invasive MRI. Nevertheless, the observed brain patterns can be readily related to the different clinical symptoms often observed in m.3243A > G patients, such as the currently high prevalence of hearing impairment. Since auditory brainstem responses are often preserved, it is likely of cochlear origin (Kullar et al., 2016). In addition, the severity of the hearing loss correlates with

the mutation load, being worse in patients with a higher mutation load (Chinnery et al., 2000). Therefore, decreasing cortical thickness and atrophy in the regions linked to auditory processing (auditory cortex, planum temporale and superior temporal sulcus and gyrus) with increasing m.3243A > G mutation load, are most likely caused by impaired cochlear functioning (Eckert et al., 2012; Formisano et al., 2008; Syka, 2002).

Even though the cortical thinning in the auditory regions may predominantly occur after cochlear damage, the morphological differences in the other affected brain regions may be induced through direct interferences of the mutation on neuronal integrity through, for example, neuronal hyperexcitability (Iizuka et al., 2003; Iizuka et al., 2002). Impaired mitochondrial protein (i.e. OXPHOS subunits) synthesis due to a defective tRNA$^{Leu(UUR)}$ has been shown in the cerebral and cerebellar cortex of post-mortem m.3243A > G brains (Sparaco et al.,

2003). Here, changes were mostly found in the intermediate layers of cGM regions, with a higher degree of cellular dependence on oxidative metabolism, and in the cerebellar Purkinje cells, respectively. As such, neuronal changes may occur especially in brain regions characterized by a high (baseline) energy demand and/or functional connectivity or cerebellum (i.e. metabolic hypothesis), depending on the mutation load similar to that observed in skeletal muscle cells (Aure et al., 2006). These high energy consuming brain areas include regions related to the default mode, dorsal attention and sensorimotor networks (Tomasi et al., 2013), in agreement with our findings of atrophy in these regions, such as in the precuneus, middle frontal gyrus and central sulcus (somatosensory and motor cortices), respectively. The cortical thinning observed in regions associated with attentional control/executive functioning, such as the middle frontal and parietal gyri and anterior cingulate cortices (Milham et al., 2002), are consistent with behavioral symptoms, e.g. patients with a higher mutation load performed worse on the Stroop task. In particular, OXPHOS deficits-susceptible inhibitory interneurons may play a prominent role in the cognitive dysfunctioning observed in mitochondrial disease patients (Finsterer, 2012; Lax et al., 2016).

Comparable to the cGM atrophy, cerebellar GM atrophy was most pronounced in the high mutation load group compared to patients with a lower mutation load, quantified by a volume loss or illustrated by larger inter-folial spaces. Previously, studies have shown that the cerebellum is highly vulnerable to mitochondrial dysfunctioning (Scaglia et al., 2005) due to respiratory chain deficiencies of complex I and IV, leading to cerebellar atrophy by Purkinje and granule cell loss (Lax et al., 2012; Sparaco et al., 2003). This is consistent with the fact that cerebellar ataxia is commonly described in mtDNA patients (de Laat et al., 2012; Lax et al., 2012). As for cerebellar GM, smaller subcortical volume was observed for the patients compared to the healthy controls, in particular in the Pu and GP (i.e. lentiform nucleus), structures especially involved in motor execution (Middleton and Strick, 2000). The volume loss correlates with the described neuronal vacuolization (i.e. spongiosis) in both these structures for several patients, potentially resulting from abnormalities within the vascular smooth muscle and endothelial cells (i.e. vascular hypothesis, Betts et al. (2006)) or from astroglial pathogenesis (Bugiani et al., 2017; van der Knaap et al., 2012). However, in contrast to the cortical and cerebellar GM, the mutation load did not affect the degree of subcortical atrophy. This may implicate that the causal mechanism is different compared to that underlying cortical atrophy (e.g. vascular vs. metabolic hypotheses). Generally, by taking together the cortical atrophy in sensorimotor regions, subcortical (i.e. lentiform nucleus) and cerebellar GM volume losses, the current results suggest a global brain-wide impaired motor functioning (Seidler et al., 2015). These changes are excellent brain correlates to some of the symptoms often observed in m.3243A > G and mitochondrial disease patients, such as cerebellar (and/or sensory) ataxia and gait instability (de Laat et al., 2012).

4.3. Cortical microstructure- and metabolic-related markers of the m.3243A > G mutation

Besides macroscopic morphological differences, T_1, T_2^* and CBF significantly varied (i.e. increased) as a function of mutation load in several cGM regions. Differences in quantitative T_1 and T_2^* across the brain are predominantly attributed to varying myelin and iron content between brain structures and regions (Stuber et al., 2014). In line with earlier work that showed delayed or decreased myelination in patients affected by respiratory chain defects (Dinopoulos et al., 2005; Lax et al., 2016; Sofou et al., 2013), positive correlations between T_1 and T_2^* values with mutation load within the patient population were observed, in particular in the primary- and heavily-myelinated regions of the cGM, including the somatosensory- and motor cortices (Haast et al., 2016), but also in cerebellar GM. In general, increased T_1 and T_2^* implicate lower levels of myelin (Stuber et al., 2014). Decreased myelin

synthesis, due to the defective cellular energy production during the critical time of myelin development in early life, may have resulted in the increasing T_1 and T_2^* with mutation load. Furthermore, we observed higher CBF in the subcortical structures as well as in the superior frontal gyrus, for patients with a higher mutation load. These effects could be induced (i) by the altered vascular functionality (e.g. related to the subcortical spongiosis and vascular abnormalities), (ii) by a compensatory mechanism for the impaired neuronal energy production or (iii) as an attempt to reduce the increased brain lactate (or other potentially harmful compounds) levels, as argued by Rodan et al. (2015).

However, when the patient populations are compared against controls, surprisingly, the metabolic-, but also microstructural-related characteristics do not follow the expected linear change as a function of mutation load, but a U-shaped dependency across groups. That is, MRI values over the entire cortex of P_{high} patients and healthy subjects are similarly different than those of the P_{low} patients. Two hypotheses could explain this observed pattern: i) the dip in cortical CBF, T_1 and T_2^* values for the P_{low} patients may signify that certain compensatory mechanisms are initiated only in the P_{high} patients (i.e. mitochondrial threshold effect). That is, for the P_{low} group, there is only a mild loss in e.g. myelination, which does not evoke/necessitate activation of local molecular pathways to compensate for this loss. However, for the P_{high} group, compensatory mechanisms are necessary to maintain functioning of the respective brain area. In fact, delayed myelination in the P_{high} group, as described above, may have led to global myelination levels similar to control ranges, as suggested by the correspondence between the range of T_1 and T_2^* values observed in the group-wise comparison between controls and patients, confirming earlier claims (Dinopoulos et al., 2005; Sofou et al., 2013). Alternatively, ii) T_1, T_2^* and brain metabolic changes have many biochemical and microscopic contributions, which do not have to follow the same dependency on mutation load. For example, T_1 increases as a function of both myelin and iron. That is, a decrease in myelin has an opposing effect on the resulting T_1 values than an increase in iron content, and the latter change is a common observation in many neurodegenerative diseases. Thus, it is reasonable to assume that myelination decreases and iron content increases as a function of mutation load but they have different dependencies on the m.3243A > G mutation load, leading to the U-shape function observed pattern for T_1. In contrast to the observed cortical pattern, the increased cerebellar GM T_1 observed in patients compared to controls, in addition to the unchanged T_2^*, may implicate predominantly myelin loss secondary to neuronal and axonal loss (Lax et al., 2012; Virtanen et al., 2011).

Interestingly, T_1 and T_2^* differences in the subcortical structures were absent, which is indicative for subcortical biochemical changes that may be more specific for certain mtDNA mutations (Barragan-Campos et al., 2005; Bindu et al., 2015). This is in sharp contrast to previously observed subcortical T_1w and T_2w changes (Tschampa et al., 2013). However, it is important to note that most of the available MRI studies on mitochondrial diseases, if not all, employed data acquired using conventional clinical, non-quantitative MRI approaches, such as FLAIR. These do not provide quantitative markers of the underlying biochemical composition of the tissue, as the MRI signal intensity are additionally influenced by MRI sequence parameters and the hardware setup (such as transmit and receive imaging coils) (Bock et al., 2013; Lorio et al., 2016). Moreover, clinical scans typically have anisotropic voxel sizes, increasing partial voluming effects and mixing signals originating from WM and GM or spongiotic tissue and subcortical GM. Therefore, quantitative interpretation of data acquired for diagnostic purposes is challenging, as interpretations of such data contributions are confounded by many other MRI acquisition and physiological parameters (e.g. transmit and receive RF fields, proton density, relaxation rates, macromolecule concentrations (Haast et al., 2016)). In summary, these results exemplify the benefits of a multi-parametric MRI protocol, as they allow discerning the biochemical causes of brain changes in disease and reliable intra- and inter-subject comparisons.

5. Conclusions

In conclusion, the current work utilized high-resolution MRI data acquired using 7T MRI to quantify brain changes in a representative population of m.3243A > G patients. The data revealed neuroradiological (i.e. morphology, microstructure- and metabolism-related) changes in patients with varying levels of mutation load, including those with a mutation load lower than previously observed threshold levels, compared to healthy controls (see Supplementary Table 2 for an overview). Interestingly, mutation load in blood compared to UECs provides a better estimate of the brain changes. The observed changes are widespread, but mainly affect GM, and are consistent with the different clinical symptoms. However, the underlying biological mechanisms and timing may vary across brain structures/regions. Our results, thus, indicate the value of quantitative MRI at 7T to determine pathological effects of the m.3243A > G mutation on brain structure and function for various mutation loads. Future longitudinal quantitative MRI but also in vitro studies are necessary to track the progression of the detected MRI-based biomarkers to improve the understanding of the disease pathogenesis and clinical symptoms development.

Acknowledgments

Appendix A. Supplementary data

Supplementary data to this article can be found online at https://doi.org/10.1016/j.nicl.2018.01.017.

References

Aure, K., Fayet, G., Leroy, J.P., Lacene, E., Romero, N.B., Lombes, A., 2006. Apoptosis in mitochondrial myopathies is linked to mitochondrial proliferation. Brain 129, 1249–1259.

Barragan-Campos, H.M., Vallee, J.N., Lo, D., Barrera-Ramirez, C.F., Argote-Greene, M., Sanchez-Guerrero, J., Estanol, B., Guillevin, R., Chiras, J., 2005. Brain magnetic resonance imaging findings in patients with mitochondrial cytopathies. Arch. Neurol. 62, 737–742.

Betts, J., Jaros, E., Perry, R.H., Schaefer, A.M., Taylor, R.W., Abdel-All, Z., Lightowlers, R.N., Turnbull, D.M., 2006. Molecular neuropathology of MELAS: level of heteroplasmy in individual neurones and evidence of extensive vascular involvement. Neuropathol. Appl. Neurobiol. 32, 359–373.

Bindu, P.S., Arvinda, H., Taly, A.B., Govindaraju, C., Sonam, K., Chiplunkar, S., Kumar, R., Gayathri, N., Bharath Mm, S., Nagappa, M., Sinha, S., Khan, N.A., Govindaraj, P., Nunia, V., Paramasivam, A., Thangaraj, K., 2015. Magnetic resonance imaging correlates of genetically characterized patients with mitochondrial disorders: a study from south India. Mitochondrion 25, 6–16.

Bock, N.A., Hashim, E., Janik, R., Konyer, N.B., Weiss, M., Stanisz, G.J., Turner, R., Geyer, S., 2013. Optimizing T1-weighted imaging of cortical myelin content at 3.0 T. NeuroImage 65, 1–12.

Bugiani, M., Dubey, M., Breur, M., Postma, N.L., Dekker, M.P., Ter Braak, T., Boschert, U., Abbink, T.E.M., Mansvelder, H.D., Min, R., van Weering, J.R.T., van der Knaap, M.S., 2017. Megalencephalic leukoencephalopathy with cysts: the Glialcam-null mouse model. Ann. Clin. Transl. Neurol. 4, 450–465.

Chinnery, P.F., Howell, N., Lightowlers, R.N., Turnbull, D.M., 1997. Molecular pathology of MELAS and MERRF. The relationship between mutation load and clinical phenotypes. Brain 120 (Pt 10), 1713–1721.

Chinnery, P.F., Elliott, C., Green, G.R., Rees, A., Coulthard, A., Turnbull, D.M., Griffiths, T.D., 2000. The spectrum of hearing loss due to mitochondrial DNA defects. Brain 123 (Pt 1), 82–92.

Chomyn, A., Martinuzzi, A., Yoneda, M., Daga, A., Hurko, O., Johns, D., Lai, S.T., Nonaka, I., Angelini, C., Attardi, G., 1992. MELAS mutation in mtDNA binding site for transcription termination factor causes defects in protein synthesis and in respiration but no change in levels of upstream and downstream mature transcripts. Proc. Natl. Acad. Sci. U. S. A. 89, 4221–4225.

Dale, A.M., Fischl, B., Sereno, M.I., 1999. Cortical surface-based analysis. I. Segmentation and surface reconstruction. NeuroImage 9, 179–194.

Dinopoulos, A., Cecil, K.M., Schapiro, M.B., Papadimitriou, A., Hadjigeorgiou, G.M., Wong, B., deGrauw, T., Egelhoff, J.C., 2005. Brain MRI and proton MRS findings in infants and children with respiratory chain defects. Neuropediatrics 36, 290–301.

Duyn, J.H., van Gelderen, P., Li, T.Q., de Zwart, J.A., Koretsky, A.P., Fukunaga, M., 2007. High-field MRI of brain cortical substructure based on signal phase. Proc. Natl. Acad. Sci. U. S. A. 104, 11796–11801.

Eckert, M.A., Cute, S.L., Vaden Jr., K.I., Kuchinsky, S.E., Dubno, J.R., 2012. Auditory cortex signs of age-related hearing loss. J. Assoc. Res. Otolaryngol. 13, 703–713.

Eggenschwiler, F., Kober, T., Magill, A.W., Gruetter, R., Marques, J.P., 2012. SA2RAGE: a new sequence for fast B1 + -mapping. Magn. Reson. Med. 67, 1609–1619.

Van der Elst, W., van Boxtel, M.P., van Breukelen, G.J., Jolles, J., 2006a. The Letter Digit Substitution Test: normative data for 1,858 healthy participants aged 24-81 from the Maastricht Aging Study (MAAS): influence of age, education, and sex. J. Clin. Exp. Neuropsychol. 28, 998–1009.

Fayssoil, A., Laforet, P., Bougouin, W., Jardel, C., Lombes, A., Becane, H.M., Berber, N., Stojkovic, T., Behin, A., Eymard, B., Duboc, D., Wahbi, K., 2017. Prediction of long-term prognosis by heteroplasmy levels of the m.3243A > G mutation in patients with the mitochondrial encephalomyopathy, lactic acidosis and stroke-like episodes syndrome. Eur. J. Neurol. 24, 255–261.

Finsterer, J., 2012. Cognitive dysfunction in mitochondrial disorders. Acta Neurol. Scand. 126, 1–11.

Fischl, B., Sereno, M.I., Tootell, R.B., Dale, A.M., 1999. High-resolution intersubject averaging and a coordinate system for the cortical surface. Hum. Brain Mapp. 8, 272–284.

Fischl, B., Salat, D.H., Busa, E., Albert, M., Dieterich, M., Haselgrove, C., van der Kouwe, A., Killiany, R., Kennedy, D., Klaveness, S., Montillo, A., Makris, N., Rosen, B., Dale, A.M., 2002. Whole brain segmentation: automated labeling of neuroanatomical structures in the human brain. Neuron 33, 341–355.

Formisano, E., De Martino, F., Bonte, M., Goebel, R., 2008. "Who" is saying "what"? Brain-based decoding of human voice and speech. Science 322, 970–973.

Frederiksen, A.L., Andersen, P.H., Kyvik, K.O., Jeppesen, T.D., Vissing, J., Schwartz, M., 2006. Tissue specific distribution of the 3243A- > G mtDNA mutation. J. Med. Genet. 43, 671–677.

Gardener, A.G., Gowland, P.A., Francis, S.T., 2009. Implementation of quantitative perfusion imaging using pulsed arterial spin labeling at ultra-high field. Magn. Reson. Med. 61, 874–882.

Goto, Y., Nonaka, I., Horai, S., 1990. A mutation in the tRNA(Leu)(UUR) gene associated with the MELAS subgroup of mitochondrial encephalomyopathies. Nature 348, 651–653.

Haast, R.A., Ivanov, D., Formisano, E., Uludag, K., 2016. Reproducibility and reliability of quantitative and weighted T1 and T2* mapping for myelin-based cortical Parcellation at 7Tesla. Front. Neuroanat. 10 (112).

Iizuka, T., Sakai, F., Suzuki, N., Hata, T., Tsukahara, S., Fukuda, M., Takiyama, Y., 2002. Neuronal hyperexcitability in stroke-like episodes of MELAS syndrome. Neurology 59, 816–824.

Iizuka, T., Sakai, F., Kan, S., Suzuki, N., 2003. Slowly progressive spread of the stroke-like lesions in MELAS. Neurology 61, 1238–1244.

Ikawa, M., Yoneda, M., Muramatsu, T., Matsunaga, A., Tsujikawa, T., Yamamoto, T., Kosaka, N., Kinoshita, K., Yamamura, O., Hamano, T., Nakamoto, Y., Kimura, H., 2013. Detection of preclinically latent hyperperfusion due to stroke-like episodes by arterial spin-labeling perfusion MRI in MELAS patients. Mitochondrion 13, 676–680.

Ivanov, D., Gardumi, A., Haast, R.A.M., Pfeuffer, J., Poser, B.A., Uludag, K., 2017a. Comparison of 3T and 7T ASL techniques for concurrent functional perfusion and BOLD studies. NeuroImage 156, 363–376.

Ivanov, D., Poser, B.A., Huber, L., Pfeuffer, J., Uludag, K., 2017b. Optimization of simultaneous multislice EPI for concurrent functional perfusion and BOLD signal measurements at 7T. Magn. Reson. Med. 78, 121–129.

Keogh, M.J., Chinnery, P.F., 2015. Mitochondrial DNA mutations in neurodegeneration. Biochim. Biophys. Acta 1847, 1401–1411.

Keuken, M.C., Bazin, P.L., Backhouse, K., Beekhuizen, S., Himmer, L., Kandola, A., Lafeber, J.J., Prochazkova, L., Trutti, A., Schafer, A., Turner, R., Forstmann, B.U., 2017. Effects of aging on T_1, T_2*, and QSM MRI values in the subcortex. Brain Struct. Funct. 222, 2487–2505.

van der Knaap, M.S., Boor, I., Estevez, R., 2012. Megalencephalic leukoencephalopathy with subcortical cysts: chronic white matter oedema due to a defect in brain ion and water homoeostasis. Lancet Neurol. 11, 973–985.

Kollia, K., Maderwald, S., Putzki, N., Schlamann, M., Theysohn, J.M., Kraff, O., Ladd, M.E., Forsting, M., Wanke, I., 2009. First clinical study on ultra-high-field MR imaging in patients with multiple sclerosis: comparison of 1.5 T and 7T. AJNR Am. J. Neuroradiol. 30, 699–702.

Kullar, P.J., Quail, J., Lindsey, P., Wilson, J.A., Horvath, R., Yu-Wai-Man, P., Gorman, G.S., Taylor, R.W., Ng, Y., McFarland, R., Moore, B.C., Chinnery, P.F., 2016. Both mitochondrial DNA and mitonuclear gene mutations cause hearing loss through cochlear dysfunction. Brain 139, e33.

de Laat, P., Koene, S., van den Heuvel, L.P., Rodenburg, R.J., Janssen, M.C., Smeitink, J.A., 2012. Clinical features and heteroplasmy in blood, urine and saliva in 34 Dutch families carrying the m.3243A > G mutation. J. Inherit. Metab. Dis. 35, 1059–1069.

Lax, N.Z., Hepplewhite, P.D., Reeve, A.K., Nesbitt, V., McFarland, R., Jaros, E., Taylor, R.W., Turnbull, D.M., 2012. Cerebellar ataxia in patients with mitochondrial DNA disease: a molecular clinicopathological study. J. Neuropathol. Exp. Neurol. 71, 148–161.

Lax, N.Z., Grady, J., Laude, A., Chan, F., Hepplewhite, P.D., Gorman, G., Whittaker, R.G.,

Ng, Y., Cunningham, M.O., Turnbull, D.M., 2016. Extensive respiratory chain defects in inhibitory interneurones in patients with mitochondrial disease. Neuropathol. Appl. Neurobiol. 42, 180–193.

Li, R., Xiao, H.F., Lyu, J.H., Wang D, J.J., Ma, L., Lou, X., 2017. Differential diagnosis of mitochondrial encephalopathy with lactic acidosis and stroke-like episodes (MELAS) and ischemic stroke using 3D pseudocontinuous arterial spin labeling. J. Magn. Reson. Imaging 45, 199–206.

Lightowlers, R.N., Taylor, R.W., Turnbull, D.M., 2015. Mutations causing mitochondrial disease: what is new and what challenges remain? Science 349, 1494–1499.

Lorio, S., Kherif, F., Ruef, A., Melie-Garcia, L., Frackowiak, R., Ashburner, J., Helms, G., Lutti, A., Draganski, B., 2016. Neurobiological origin of spurious brain morphological changes: a quantitative MRI study. Hum. Brain Mapp. 37, 1801–1815.

Magistretti, P.J., Allaman, I., 2015. A cellular perspective on brain energy metabolism and functional imaging. Neuron 86, 883–901.

Marques, J.P., Kober, T., Krueger, G., van der Zwaag, W., Van de Moortele, P.F., Gruetter, R., 2010. MP2RAGE, a self bias-field corrected sequence for improved segmentation and T1-mapping at high field. NeuroImage 49, 1271–1281.

Middleton, F.A., Strick, P.L., 2000. Basal ganglia and cerebellar loops: motor and cognitive circuits. Brain Res. Brain Res. Rev. 31, 236–250.

Milham, M.P., Erickson, K.I., Banich, M.T., Kramer, A.F., Webb, A., Wszalek, T., Cohen, N.J., 2002. Attentional control in the aging brain: insights from an fMRI study of the stroop task. Brain Cogn. 49, 277–296.

Nakada, T., Matsuzawa, H., Igarashi, H., Fujii, Y., Kwee, I.L., 2008. In vivo visualization of senile-plaque-like pathology in Alzheimer's disease patients by MR microscopy on a 7T system. J. Neuroimaging 18, 125–129.

Nesbitt, V., Pitceathly, R.D., Turnbull, D.M., Taylor, R.W., Sweeney, M.G., Mudanohwo, E.E., Rahman, S., Hanna, M.G., McFarland, R., 2013. The UK MRC Mitochondrial Disease Patient Cohort Study: clinical phenotypes associated with the m.3243A > G mutation–implications for diagnosis and management. J. Neurol. Neurosurg. Psychiatry 84, 936–938.

Norris, D.G., 2003. High field human imaging. J. Magn. Reson. Imaging 18, 519–529.

Pfeuffer, J., van de Moortele, P.F., Yacoub, E., Shmuel, A., Adriany, G., Andersen, P., Merkle, H., Garwood, M., Ugurbil, K., Hu, X., 2002. Zoomed functional imaging in the human brain at 7Tesla with simultaneous high spatial and high temporal resolution. NeuroImage 17, 272–286.

Pohmann, R., Speck, O., Scheffler, K., 2016. Signal-to-noise ratio and MR tissue parameters in human brain imaging at 3, 7, and 9.4 tesla using current receive coil arrays. Magn. Reson. Med. 75, 801–809.

Rahman, S., Poulton, J., Marchington, D., Suomalainen, A., 2001. Decrease of 3243 A–> G mtDNA mutation from blood in MELAS syndrome: a longitudinal study. Am. J. Hum. Genet. 68, 238–240.

Rajasimha, H.K., Chinnery, P.F., Samuels, D.C., 2008. Selection against pathogenic mtDNA mutations in a stem cell population leads to the loss of the 3243A–> G mutation in blood. Am. J. Hum. Genet. 82, 333–343.

Reeve, A.K., Krishnan, K.J., Turnbull, D., 2008. Mitochondrial DNA mutations in disease, aging, and neurodegeneration. Ann. N. Y. Acad. Sci. 1147, 21–29.

Rodan, L.H., Poublanc, J., Fisher, J.A., Sobczyk, O., Wong, T., Hlasny, E., Mikulis, D., Tein, I., 2015. Cerebral hyperperfusion and decreased cerebrovascular reactivity correlate with neurologic disease severity in MELAS. Mitochondrion 22, 66–74.

Romero, J.E., Coupe, P., Giraud, R., Ta, V.T., Fonov, V., Park, M.T., Chakravarty, M.M., Voineskos, A.N., Manjon, J.V., 2017. CERES: a new cerebellum lobule segmentation method. NeuroImage 147, 916–924.

Rossignol, R., Faustin, B., Rocher, C., Malgat, M., Mazat, J.P., Letellier, T., 2003. Mitochondrial threshold effects. Biochem. J. 370, 751–762.

Sallevelt, S.C., Dreesen, J.C., Drusedau, M., Spiers, S., Coonen, E., van Tienen, F.H., van Golde, R.J., de Coo, I.F., Geraedts, J.P., de Die-Smulders, C.E., Smeets, H.J., 2013. Preimplantation genetic diagnosis in mitochondrial DNA disorders: challenge and success. J. Med. Genet. 50, 125–132.

Saneto, R.P., Friedman, S.D., Shaw, D.W., 2008. Neuroimaging of mitochondrial disease. Mitochondrion 8, 396–413.

Scaglia, F., Wong, L.J., Vladutiu, G.D., Hunter, J.V., 2005. Predominant cerebellar volume loss as a neuroradiologic feature of pediatric respiratory chain defects. AJNR Am. J. Neuroradiol. 26, 1675–1680.

Schaefer, A.M., Phoenix, C., Elson, J.L., McFarland, R., Chinnery, P.F., Turnbull, D.M., 2006. Mitochondrial disease in adults: a scale to monitor progression and treatment. Neurology 66, 1932–1934.

Seidler, R., Erdeniz, B., Koppelmans, V., Hirsiger, S., Merillat, S., Jancke, L., 2015. Associations between age, motor function, and resting state sensorimotor network connectivity in healthy older adults. NeuroImage 108, 47–59.

Shanske, S., Pancrudo, J., Kaufmann, P., Engelstad, K., Jhung, S., Lu, J., Naini, A., DiMauro, S., De Vivo, D.C., 2004. Varying loads of the mitochondrial DNA A3243G

mutation in different tissues: implications for diagnosis. Am. J. Med. Genet. A 130A, 134–137.

Sofou, K., Steneryd, K., Wiklund, L.M., Tulinius, M., Darin, N., 2013. MRI of the brain in childhood-onset mitochondrial disorders with central nervous system involvement. Mitochondrion 13, 364–371.

Sokoloff, L., Reivich, M., Kennedy, C., Des Rosiers, M.H., Patlak, C.S., Pettigrew, K.D., Sakurada, O., Shinohara, M., 1977. The [14C]deoxyglucose method for the measurement of local cerebral glucose utilization: theory, procedure, and normal values in the conscious and anesthetized albino rat. J. Neurochem. 28, 897–916.

Sparaco, M., Simonati, A., Cavallaro, T., Bartolomei, L., Grauso, M., Piscioli, F., Morelli, L., Rizzuto, N., 2003. MELAS: clinical phenotype and morphological brain abnormalities. Acta Neuropathol. 106, 202–212.

Stuber, C., Morawski, M., Schafer, A., Labadie, C., Wahnert, M., Leuze, C., Streicher, M., Barapatre, N., Reimann, K., Geyer, S., Spemann, D., Turner, R., 2014. Myelin and iron concentration in the human brain: a quantitative study of MRI contrast. NeuroImage 93 (Pt 1), 95–106.

Syka, J., 2002. Plastic changes in the central auditory system after hearing loss, restoration of function, and during learning. Physiol. Rev. 82, 601–636.

Teeuwisse, W.M., Brink, W.M., Webb, A.G., 2012. Quantitative assessment of the effects of high-permittivity pads in 7Tesla MRI of the brain. Magn. Reson. Med. 67, 1285–1293.

Tomasi, D., Wang, G.J., Volkow, N.D., 2013. Energetic cost of brain functional connectivity. Proc. Natl. Acad. Sci. U. S. A. 110, 13642–13647.

Trattnig, S., Springer, E., Bogner, W., Hangel, G., Strasser, B., Dymerska, B., Cardoso, P.L., Robinson, S.D., 2016. Key clinical benefits of neuroimaging at 7T. NeuroImage 30651–30656 pii: S1053-8119.

Tschampa, H.J., Urbach, H., Greschus, S., Kunz, W.S., Kornblum, C., 2013. Neuroimaging characteristics in mitochondrial encephalopathies associated with the m.3243A > G MTTL1 mutation. J. Neurol. 260, 1071–1080.

Tsujikawa, T., Yoneda, M., Shimizu, Y., Uematsu, H., Toyooka, M., Ikawa, M., Kudo, T., Okazawa, H., Kuriyama, M., Kimura, H., 2010. Pathophysiologic evaluation of MELAS strokes by serially quantified MRS and CASL perfusion images. Brain and Development 32, 143–149.

Tsujikawa, K., Senda, J., Yasui, K., Hasegawa, Y., Hoshiyama, M., Katsuno, M., Sobue, G., 2016. Distinctive distribution of brain volume reductions in MELAS and mitochondrial DNA A3243G mutation carriers: a voxel-based morphometric study. Mitochondrion 30, 229–235.

Ugurbil, K., 2017. Imaging at ultrahigh magnetic fields: history, challenges, and solutions. Neuroimage 30575-X pii: S1053-8119.

Uludag, K., Blinder, P., 2017. Linking brain vascular physiology to hemodynamic response in ultra-high field fMRI. NeuroImage 30175–301751 pii: S1053-8119.

Van der Elst, W., van Boxtel, M.P., van Breukelen, G.J., Jolles, J., 2005. Rey's verbal learning test: normative data for 1855 healthy participants aged 24-81 years and the influence of age, sex, education, and mode of presentation. J. Int. Neuropsychol. Soc. 11, 290–302.

Van der Elst, W., Van Boxtel, M.P., Van Breukelen, G.J., Jolles, J., 2006b. The Stroop color-word test: influence of age, sex, and education; and normative data for a large sample across the adult age range. Assessment 13, 62–79.

Vaughan, J.T., Garwood, M., Collins, C.M., Liu, W., DelaBarre, L., Adriany, G., Andersen, P., Merkle, H., Goebel, R., Smith, M.B., Ugurbil, K., 2001. 7T vs. 4 T: RF power, homogeneity, and signal-to-noise comparison in head images. Magn. Reson. Med. 46, 24–30.

Virtanen, S.M., Lindroos, M.M., Majamaa, K., Nuutila, P., Borra, R.J., Parkkola, R., 2011. Voxelwise analysis of diffusion tensor imaging and structural MR imaging in patients with the m.3243A > G mutation in mitochondrial DNA. AJNR Am. J. Neuroradiol. 32, 522–526.

Whittaker, R.G., Blackwood, J.K., Alston, C.L., Blakely, E.L., Elson, J.L., McFarland, R., Chinnery, P.F., Turnbull, D.M., Taylor, R.W., 2009. Urine heteroplasmy is the best predictor of clinical outcome in the m.3243A > G mtDNA mutation. Neurology 72, 568–569.

Yacoub, E., Harel, N., Ugurbil, K., 2008. High-field fMRI unveils orientation columns in humans. Proc. Natl. Acad. Sci. U. S. A. 105, 10607–10612.

Yushkevich, P.A., Piven, J., Hazlett, H.C., Smith, R.G., Ho, S., Gee, J.C., Gerig, G., 2006. User-guided 3D active contour segmentation of anatomical structures: significantly improved efficiency and reliability. NeuroImage 31, 1116–1128.

Zhu, X.H., Qiao, H., Du, F., Xiong, Q., Liu, X., Zhang, X., Ugurbil, K., Chen, W., 2012. Quantitative imaging of energy expenditure in human brain. NeuroImage 60, 2107–2117 (s).

van der Zwaag, W., Schafer, A., Marques, J.P., Turner, R., Trampel, R., 2016. Recent applications of UHF-MRI in the study of human brain function and structure: a review. NMR Biomed. 29, 1274–1288.